OFFICE OF NAVAL RESEARCH

Contract N00014-75-C-0349 NR 031-754
AFOSR-78-3471

GIT-TR-78-1

TECHNICAL REPORT 78-1

# QUANTITATIVE STEREOLOGICAL METHODS FOR ANALYZING IMPORTANT MICROSTRUCTURAL FEATURES IN FATIGUE OF METALS AND ALLOYS.

E. E. UNDERWOOD and E. A. STARKE, JR.

~~April 6, 1978~~
6 Apr 78

142 p.

METALLURGY PROGRAM, SCHOOL OF CHEMICAL ENGINEERING
GEORGIA INSTITUTE OF TECHNOLOGY
ATLANTA, GEORGIA 30332



409 996

# QUANTITATIVE STEREOLOGICAL METHODS FOR ANALYZING IMPORTANT MICROSTRUCTURAL FEATURES IN FATIGUE OF METALS AND ALLOYS

E. E. Underwood and E. A. Starke, Jr.
School of Chemical Engineering and Metallurgy
Georgia Institute of Technology
Atlanta, Georgia 30332

ABSTRACT: This paper reviews the practical aspects of extracting quantitative microstructural data from fatigue microstructures. In addition to the basic stereological information needed to characterize the essential elements of the structure, special methods are developed and described for quantifying more subtle effects. Thus, elongated structures, lamellar systems, gradients, and locational characteristics of particles are considered with respect to the fatigue process and its interactions with the microstructural features.

One of the primary goals of the materials scientist is to be able to design alloys for specific engineering applications using basic principles instead of trial and error methods. To reach this goal a thorough knowledge of the quantitative relationships between microstructure and engineering properties must be obtained. Considerable progress has been made in correlating microstructure with monotonic properties which involve gross yielding, such as yield strength and fracture toughness. However, our understanding of the quantitative effects of various microstructural features on both fatigue crack initiation and propagation is still lagging. The main difficulty can be attributed to the localized nature of the fatigue processes, and the fact that the important microstructural features are often heterogeneous. Thus they are more difficult to quantify than the generally uniform features that control the gross yielding process.

The routine stereological analysis of the statistically-uniform microstructural features[1] is of definite value, not only for the sake of describing the type of alloy with which one is dealing, but also because any further quantification will require a quantitative base. First we describe methods for obtaining quantitatively the volume, surface area, line length and number density of features in typical fatigue microstructures. Both manual and automatic image analyses are employed. Next, we extract additional quantitative information that bears on the more intangible

concepts, such as shape, orientation, and gradient effects. Also investigated are methods for improving the quantitative treatment of fracture surfaces, particle randomness or segregation, and the projected images obtained from transmission electron microscopy (TEM). This is a difficult task, since sampling techniques, metallographic procedures, and stereological theory have not yet been fully worked out for these more specialized applications. However, much can be done at the present time to place the fatigue process on a closer quantitative basis with the alloy microstructure.

## BASIC STEREOLOGICAL CHARACTERIZATION OF A MICROSTRUCTURE

Before it is possible to devise new techniques for the quantitative description of a particular microstructural feature, it is necessary to know quantitatively the basic characteristics of the microstructure. The measurements required for a basic characterization are fewer than generally realized. In the example chosen here for analysis, there are only three measurements to make, and they are all simple counting-type measurements.

Figure 1 shows a fairly equiaxed grain structure with largely spherical particles embedded in the matrix as well as the grain boundaries. Quantities of interest here that can be obtained without assumptions are $S_V$, the grain boundary area per unit test volume; $L_A$, the length of grain boundary traces per unit test area; $\bar{L}$, the mean grain (or particle) intercept length; $N_A$, the number of grains (or particles) per unit test area; Q, the aspect ratio of non-equiaxed grains, $\bar{L}_{\parallel}/\bar{L}_{\perp}$; $\bar{A}$, the mean grain (or particle) intercept area; $(N_A)_b$, the number of grain boundary particles per unit test area; and $N_\ell$, the number of boundary particles per unit length of grain-boundary traces. If the assumption is made that the particles are spheres of one diameter, we can also calculate $N_V$, the number of particles per unit test volume; D, the sphere diameter; and $N_S$, the number of boundary particles per unit area of the grain boundaries. Note that $S_V$, $L_A$, $N_V$, etc. represent fractions; for example, $S_V = S/V_T$, $L_A = L/A_T$, and $P_L = P/L_T$ where $V_T$, $A_T$, and $L_T$ are the test volume, test area, and test line length, respectively.

The microstructure in Figure 1 was subjected to a point intercept density count $P_L$; a point count, $P_P$; and a grain and particle count, N. A square net grid (5 cm X 5 cm) was applied repeatedly to the microstructure to get average values of $P_L$ and $P_P$, and grains and particles were counted within a selected test area. The intersections of the grid lines give 6X6 points for the point count, while the 6 horizontal lines and 6 vertical lines constitute the test line length, $L_T$. Since

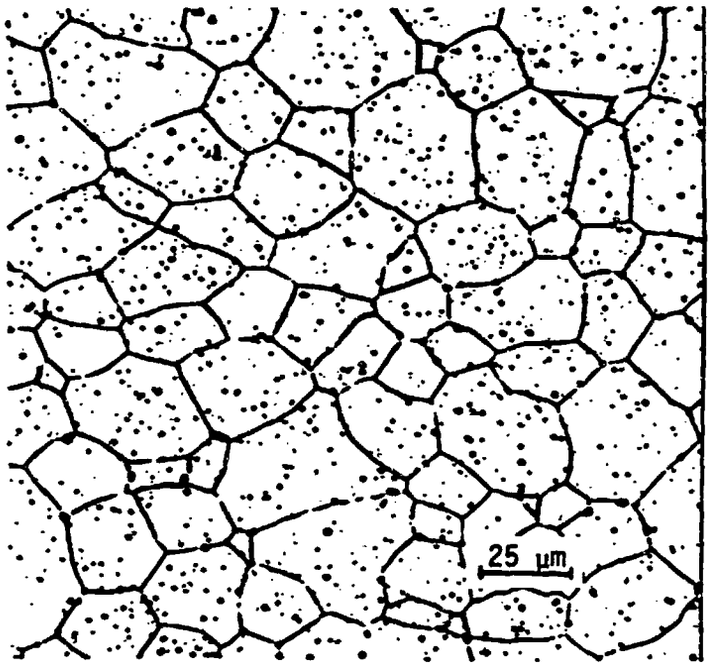


FIG. 1-Light micrograph of an Al-5Mg-0.4Ag alloy illustrating equiaxed grain structure and spherical precipitates.


FIG. 2-Light micrograph illustrating mixed recrystallized (light) and unrecrystallized (dark) structure of commercially processed 7050-T6X1 plate. Etched in 25% $HNO_3$ for 3 min. at 70°C.

the magnification of the microstructure is 500X, $L_T$ = (6X5 + 6X5)/500 = 0.12 cm and the 5 cm X 5 cm test area $A_T = 25/500^2 = 10^{-4}cm^2$.

The results of the three counting operations performed on the grains and particles are given in Table 1. The numerical data are enterd first, then these are processed into fractional form, and finally the microstructural quantities are calculated. One of the results obtained shows that there is a slight elongation of the grains (Q = 1.29) in the horizontal direction. Fortunately, however, the mean intercept length $\bar{L}$ is valid regardless of grain shape, size, or orientation, and gives a single value for any particular microstructure. This is an important grain size parameter, and best represents the physical realities of a crack or dislocations moving through an aggregate of grains. The rather artificial concept of a "diameter" (which only has significance for a sphere), implies that only the maximum dimension of a grain is involved in a particular process. If the assumption of a particular grain shape becomes necessary, tabulations are available showing the relationship of $\bar{L}$ to some characteristic dimension of the assumed figure. (For example, $\bar{L} = (2/3)\ D_{sphere}$; $\bar{L} = (2/3)\ a_{cube\ edge}$; $\bar{L} = (1.69)a_{TKDH\ edge}$; etc.) Moreover, $\bar{L}$ is directly related to both $S_V$ and $L_A$, as well as the specific surface of particles or grains, $\bar{S}/\bar{V}$. It is not readily apparent, perhaps, but $\bar{L}_2$ (the two-dimensional mean intercept length) is also equal to $\bar{L}_3$ (the three-dimensional mean intercept length). Thus there is a direct link between the section plane and the true microstructural quantities. Other results of interest in Table 1 are the particle density on grain boundaries ($N_S$) and the number of particles per unit volume ($N_V$), the calculation of which usually involves an assumption of a particular particle shape.

Another type of spacing that is used occasionally is the mean nearest neighbor spacing between particles or other features. Although many such spacings can be defined, there are only two rigorously correct expressions for point particles randomly located in a plane or in a volume[1], i.e.,

$$\Delta_2 = \tfrac{1}{2}\ P_A^{-\frac{1}{2}} \qquad (1)$$

and

$$\Delta_3 = 0.544\ P_V^{-1/3} \qquad (2)$$

where $\Delta_2$ and $\Delta_3$ are the mean two-dimensional and three-dimensional nearest neighbor spacings, respectively, and $P_A$ and $P_V$ are the number of randomly located points in a plane, per unit area, and in space, per unit volume, respectively. From practical considerations, if the particles are small, we may substitute $N_A$ for $P_A$ and $N_V$ for $P_V$ without too much loss in accuracy.

Other relationships have been derived. For the planar distribution of inclusions in a fracture surface and in a section plane, Passoja and Hill[2] derive

$$\bar{r} = \frac{\sqrt{\pi}}{2} N_S^{-1/2} \tag{3}$$

where their $N_S$ is the number of particles per unit surface area. In order to relate to dimple spacings, they use an expression due to Kocks[3]

$$D_S = 1.18\, N_S^{-1/2} \tag{4}$$

which takes into account the average distance $D_S$ between a particle and the 2d or 3d nearest neighbors. This equation was used in an attempt to characterize particle spacings in a volume adjacent to the crack tip.

Since $N_V$ is hard to obtain, we use the general relationship $N_V = N_A/\bar{D}$, and substitute in Eq. (2) (with $P_V = N_V$), which results in

$$\Delta_3 = 0.544\, \bar{D}^{1/3}\, N_A^{-1/3}. \tag{5}$$

If $\bar{D}$ can be estimated, the relatively simple $N_A$ measurement can be used in the calculation of the three-dimensional $\Delta_3$ spacing.

A microstructure commonly encountered in fatigue studies is the partially- or completely-recrystallized structure[4]. In addition to the recrystallized regions there may also be cold-worked regions, sub-grain structure, particles, and anisotropic effects such as layering and grain elongation.

A typical partially-recrystallized microstructure is seen in Figure 2. Because of the good contrast between recrystallized (light) and unrecrystallized regions (dark), the area fraction was determined both manually and automatically with the Bausch and Lomb Feature Analysis System (FAS). A comparison of results reveals that $P_P = 0.44$ ($= A_A = V_V$) was obtained with a 6X6 point grid, and the automatic measurements with the FAS gave an average value of 0.428. The areas selected for measurement were not the same, however, since the FAS sampled the entire metallographic specimen surface.

## CHARACTERIZATION OF ANISOTROPIC MICROSTRUCTURES

The microstructure shown in Figure 1 is representative of the usual equiaxed metallic or ceramic material, except perhaps for the large incidence of grain-boundary particles. Another microstructure, typical of metal working operations, is shown in Figure 3. The flattened, elongated grain structure is frequently encountered in alloys in which fatigue is important. There are several microstructural parameters that have proved useful for these elongated structures. One is a measure of the <u>mean</u> grain size $\bar{L}_3$, i.e., the mean intercept length for

TABLE 1-Procedure for determining basic microstructural data from Figure 1.

($P_T = 36$, $L_T = 0.12$ cm, $A_T = 10^{-4}$ cm$^2$)

GRAINS

$P_L$ measurement (horizontal direction designated $\parallel$):

P (hor. only) = 28 $\quad (P_L)_\parallel = P_{hor}/L_T = 28/0.06 = 466.7$ cm$^{-1}$

P (vert. only) = 36 $\quad (P_L)_\perp = P_{vert}/L_T = 36/0.06 = 600.0$ cm$^{-1}$

P (total) = 64 $\quad P_L = 64/0.12 = 533.3$ cm$^{-1}$

$L_A = (\pi/2)P_L = 1.571\ (533.3) = 837.8$ cm$^{-1}$

$S_V = 2\ P_L = 2\ (533.3) = 1066.7$ cm$^{-1}$

$\bar{L} = 1/N_L = 1/P_L = 1/533.3 = 1.87 \cdot 10^{-3}$ cm

$Q = \bar{L}_\parallel/\bar{L}_\perp = (P_L)_\perp/(P_L)_\parallel = 600/466.7 = 1.29$

N (grain counts):

$N_{interior} = 13$

$N_{boundary} = 18$ $\quad N_{total} = N_i + \frac{1}{2} N_b = 13 + (\frac{1}{2})18 = 22$

$N_A = N_{total}/A_T = 22/10^{-4} = 22 \cdot 10^4$ cm$^{-2}$

$\bar{A} = 1/N_A = 1/22 \cdot 10^4 = 4.55 \cdot 10^{-6}$ cm$^2$

PARTICLES

$P_P$ measurement (point count):

P (hitting matrix particles) = 4

$P_T$ (total grid points) = 36

$P_P = 4/36 = 0.11$ ($= A_A = V_V$)

N (particle counts):

$N_{matrix} = 546$

$N_A = N_m/A_T = 546/10^{-4} = 5.46 \cdot 10^6$ cm$^{-2}$

$\bar{A} = A_A/N_A = 0.11/5.46 \cdot 10^6 = 2.01 \cdot 10^{-8}$ cm$^2$

$N_b$ (at grain boundaries) = 64

$(N_A)_b = N_b/A_T = 64/10^{-4} = 64 \cdot 10^4$ cm$^{-2}$

$N_\ell = (N_A)_b/L_A = 64 \cdot 10^4/837.8 = 764$ cm$^{-1}$

For spherical particles of diameter D:

$\bar{A} = (2/3)\ A_{max} = (\pi/6)D^2$; $D^2 = (6/\pi)(2.01 \cdot 10^{-8})$; $D = 1.96 \cdot 10^{-4}$ cm

$N_V = N_A/D = 5.46 \cdot 10^6/1.96 \cdot 10^{-4} = 2.79 \cdot 10^{10}$ cm$^{-3}$

$N_S = DN_V = (1.96 \cdot 10^{-4})\ 2.79 \cdot 10^{10} = 5.47 \cdot 10^6$ cm$^{-2}$

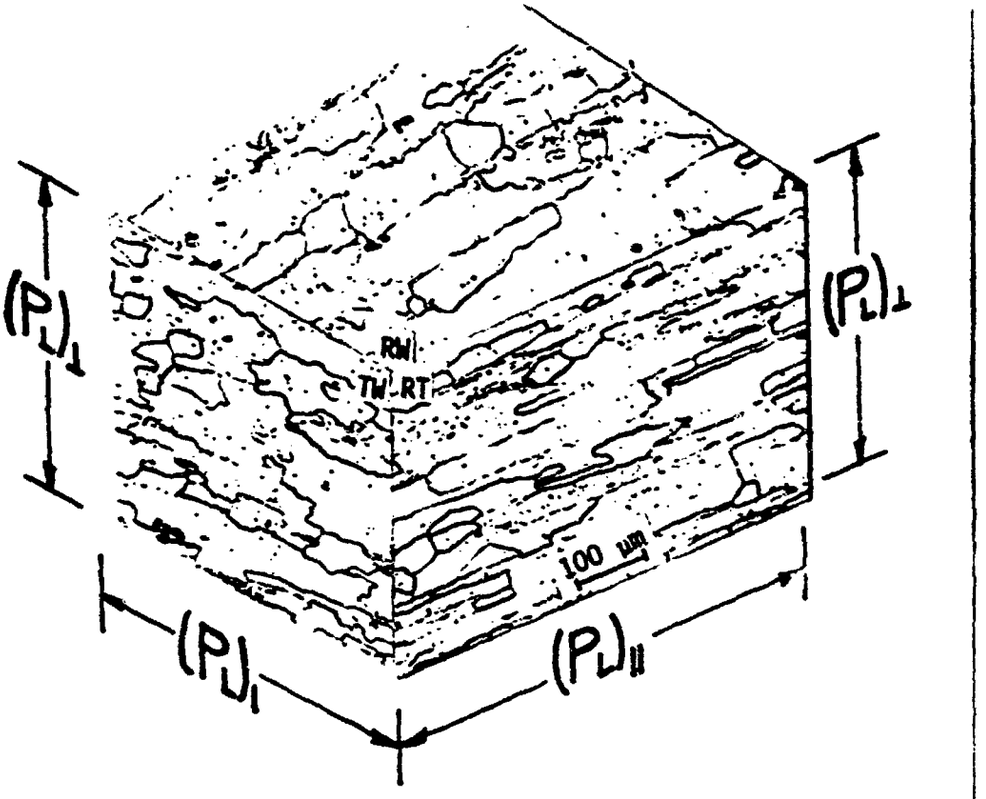


FIG. 3-Microstructure of commercially processed 7050-T6X1 plate. Keller's etch.

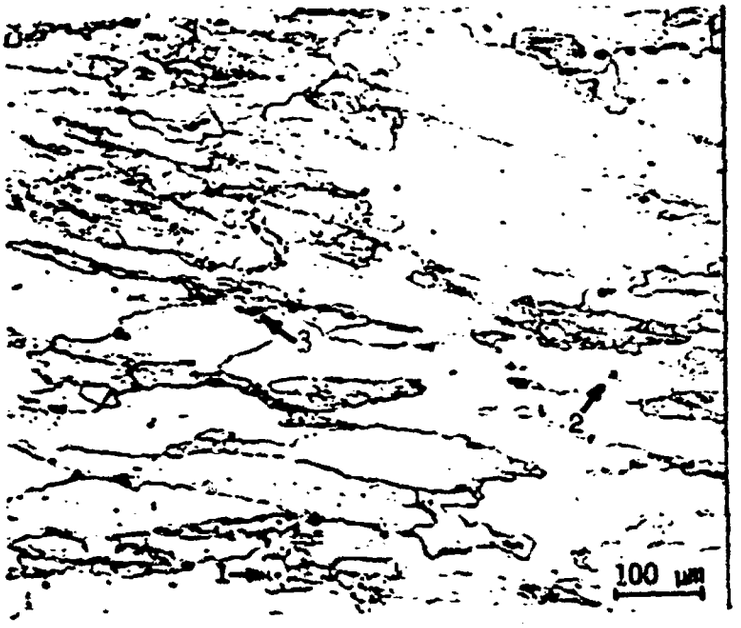


FIG. 4-Microstructure of the TW section of a wrought Al-6Zn-1Cu-0.12Zr alloy. Keller's etch.

the three-dimensional grains; another is a shape parameter, the degree of orientation $\Omega_{23}$ for surfaces (2) in a volume (3); and a third is a directional spacing parameter, such as the mean distance $\overline{L(\theta,\phi)}$ between grain boundaries or other obstacles, in some specified direction.

The mean value of intercept length for a planar-linear system of surfaces (which is the system seen in Figure 3) can be determined according to

$$\bar{P}_L = 1/3\{(P_L)_{\parallel} + (P_L)_{|} + (P_L)_{\perp}\} = 1/\bar{L}_3 \qquad (6)$$

where the directions of the $P_L$ measurements parallel ( $\parallel$ and | ) and perpendicular ($\perp$) to an orientation plane are specified graphically in Figure 3. Also, the average grain volume can be calculated from the product of the three mean intercept lengths by the equation

$$\bar{V} = (\bar{L}_{\parallel})\ (\bar{L}_{|})\ (\bar{L}_{\perp}) = \frac{1}{(P_L)_{\parallel}\ (P_L)_{|}\ (P_L)_{\perp}} . \qquad (7)$$

Or, if the diameter of an equivalent sphere of the same volume is required

$$D_{eq} = \{(\tfrac{6}{\pi})\ \bar{V}\}^{1/3} . \qquad (8)$$

As before, the mean intercept length is still related to $S_V$ through $2/\bar{L}_3$, and to $L_A$ through $(\pi/2)/\bar{L}_3$.

For the particular system of oriented surfaces in our example--the planar-linear type--the degree of orientation is designated by $\Omega_{pl\text{-}lin}$. The value of this shape parameter varies between 0 and 1, representing respectively a complete lack of orientation, and completely oriented surface elements of the system. In between, of course, we have the intermediate condition called a partially-oriented system of surfaces.

The three orthogonal $P_L$ measurements indicated by the isometric view were obtained in suitable directions from two photomicrographs of each plane. In order to indicate the amount of spread obtained, the individual values are indicated below in Table 2.

The working equation for $\Omega_{pl\text{-}lin} = (S_V)_{oriented}/(S_V)_{total}$, where $(S_V)_{oriented} = (S_V)_{planar} + (S_V)_{linear}$. Since the derivation has been given elsewhere[1], the final expression for the total oriented surfaces is merely stated here:

$$\Omega_{pl\text{-}lin} = \frac{(P_L)_{\perp} - 1.571\ (P_L)_{\parallel} + 0.571\ (P_L)_{|}}{(P_L)_{\perp} + 0.429\ (P_L)_{\parallel} + 0.571\ (P_L)_{|}} \qquad (9)$$

Substituting the three average values of $(P_L)_{\perp}$, $(P_L)_{\parallel}$ and $(P_L)_{|}$ from Table 2 yields the answer, $\Omega_{pl\text{-}lin} = 69\%$. This means that 69% of the total grain boundary

TABLE 2-Basic microstructural data for calculation of $\Omega_{pl-lin}$ and $\Omega_{12}$.

| | RT-Plane | | TW-Plane | |
|---|---|---|---|---|
| | $(P_L)_{\parallel}$ | $(P_L)_{\perp}$ | $(P_L)_{\perp}$ | $(P_L)_{\parallel}$ |
| Photo 1 | 54.4 | 204.2 | 216.7 | 111.1 |
| Photo 2 | 48.9 | 277.1 | 289.6 | 118.9 |
| Average | 51.7cm$^{-1}$ | 240.6 | 253.1 | 115.0cm$^{-1}$ |
| Avg. $(P_L)_{\perp}$ | ..... 246.9 cm$^{-1}$ | | | |

surface area is oriented parallel to the orientation plane (the horizonal plane in Figure 3). Successive changes in the microstructure as the result of further rolling, or annealing, can be followed by the new values of $\Omega_{pl-lin}$.

Another shape parameter that performs essentially the same function as $\Omega_{pl-lin}$ is the two-dimensional degree of orientation $\Omega_{12}$, which measures the orientation of grain boundary traces (or lines, 1) in a plane (2). Since the analysis requires only one plane, the amount of labor is considerably less. The working equation in this case is

$$\Omega_{12} = \frac{(P_L)_\perp - (P_L)_{//}}{(P_L)_\perp + 0.571\,(P_L)_{//}} = \frac{(L_A)_{oriented}}{(L_A)_{total}} \qquad (10)$$

By substituting appropriate values from Table 2, we find that $\Omega_{12} = 71\%$. This is quite close to $\Omega_{pl-lin}$. In fact, a direct proportionality was observed experimentally in a study of foamed rubber cell structures between $\Omega_{pl-lin}$ and $\Omega_{12}$ for a number of specimens. If this finding proves valid for metallic specimens, then considerable saving in time and effort could be achieved. However, the planar-linear analysis does provide more information than the simpler two-dimensional treatment and may be required in some cases.

Directionality effects are frequently important, per se, and this is especially so in planar-linear structures. For example, in studies of crack growth in different directions, a linear parameter that reflects the mean spacing between barriers, in the same direction as the CPD, would have fundamental significance. The parameter of choice in many such cases would be the mean intercept length in the chosen direction. Thus, for crack growth studies in the short transverse direction in the transverse plane, we would need $\bar{L}_\perp$ (see Figure 3). Provided grain boundaries were the only significant barrier, $\bar{L}$ can be calculated from $(P_L)_\perp = 246.9\ cm^{-1}$ (from Table 2), since $\bar{L}_\perp = 1/(P_L)_\perp = 4.05 \cdot 10^{-3} cm$. For crack growth in other directions $(\theta,\psi)$, we could calculate the corresponding value of $\overline{L(\theta,\psi)}$, as required. If the important barriers proved to be layers of unrecrystallized material, or layers of fine recrystallized grains, their mean spacings could be calculated as readily as for the case of grain boundaries.

Another partially-recrystallized microstructure selected for examination is shown in Figure 4. This structure is considerably more complex than the first example, and several features are of interest. For example, the area fraction of recrystallized regions, their number, and their association with particles can influence the fatigue process. Because this is an anisotropic structure, the mean spacing perpendicular to the recrystallized lamellae is of interest, as is the

mean spacing of grain boundaries normal to the crack growth direction. Other characteristics are also useful from time to time, such as the degree of orientation and the contiguity of particles and recrystallized regions. The results obtained from this microstructure are summarized below.

The area fraction of recrystallized regions was measured by point counting, using a 6X6 point grid applied repeatedly to the microstructure at random locations and at random angles. The results gave $P_p = 77/864 = 0.089$. Next, the mean spacings of the recrystallized lamellae, as well as the grain boundaries, were obtained in a direction normal to the orientation axis (horizontal direction). The applicable equation here for the lamellae is $(\bar{L})_\perp = 1/(N_L)_\perp$, where $(N_L)_\perp$ is the number of recrystallized layers intercepted per unit length of test lines normal to the orientation axis. For grain boundaries, we use $(\bar{L})_\perp = 1/(P_L)_\perp$ because the test lines are intersecting boundaries at a point. The results gave $(\bar{L}_\perp)_{lam} = 1/101.7\ cm^{-1} = 98\ \mu m$ for the lamellae, and $(\bar{L}_\perp)_{gb} = 1/423.3\ cm^{-1} = 24\ \mu m$ for the grain boundaries. A factor of over 4 times in spacing should help to reveal which barrier is the more important to crack growth.

Another outstanding attribute of this microstructure is its strong directionality. Therefore, the degree of orientation $\Omega_{12}$ of boundary lines was calculated according to Eq. (10) from values for $(P_L)_\perp = 258.3\ cm^{-1}$ and $(P_L)_{//} = 123.5\ cm^{-1}$. The result, $\Omega_{12} = 41\%$, demonstrates a strong directionality of boundaries in the rolling direction.

One further facet of this structure was investigated. A strong correspondence was noted between particles (dark areas) and recrystallized regions in that particles were frequently observed embedded within, or contiguous to, recrystallized grains. A direct count of discrete, separated recrystallized regions totalled 90, while a count of associated particles yielded 64. Thus, 71 percent of the recrystallized clumps were associated with particles. Also of interest in this connection is the "contiguity" of particles and recrystallized grains. This parameter can be expressed to give the ratio of interface area shared between particles (P) and recrystallized regions (R), compared to the total particle interface area (PR + PM), where M means the "matrix" (or the balance of the microstructure). Thus we write the contiguity of separated particles as

$$C_{PR} = \frac{(S_V)_{PR}}{(S_V)_{total\ P}} = \frac{(S_V)_{PR}}{(S_V)_{PR} + (S_V)_{PM}} \tag{11}$$

or

$$C_{PR} = \frac{(P_L)_{PR}}{(P_L)_{PR} + (P_L)_{PM}} . \tag{12}$$

In order to measure these quantities, a grid of parallel test lines is laid randomly over the microstructure, and the points of intersection with PR and PM interfaces counted separately. The three arrows in Figure 4 indicate the three possible types of particle interface combinations of interest here. One arrow points to a particle completely surrounded by a recrystallized grain (PR interface); another particle is completely surrounded by the matrix (PM interface); and the third particle is partially shared by recrystallized region and matrix (PR and PM interfaces). The contiguity parameter has demonstrated its usefulness in studies of crack propagation and fracture; it should prove equally valuable in fatigue studies.

A final topic to be discussed in this Section is that of assessing the degree of randomness, or lack of randomness, of particle locations in a plane. The two photomicrographs shown in Figure 5 are taken for examples. Pronounced "stringering" of particles is noted in the RT-plane with somewhat less layering effect in the TW-plane, which is a section normal to the RT-plane.

In order to obtain quantitative information on the degree of positional randomness, the particle locations are compared with those of a hypothetical statistically-uniform distribution, and evaluated numerically by the $\chi^2$ test for goodness of fit. The density of particles were determined within a 8 by 12 grid of 1 cm square "cells" placed over the photomicrograph. For each of these 80 cells, the number of particles were counted separately and the cell densities recorded. Since the particles exhibited a preferential alignment, a modified cell was devised in which the basic square cell data were amalgamated into 8 horizontal strips each consisting of 10 of the original square cells. This new cell configuration, in which the cells are parallel to the stringers, can more easily reflect the physical realities of the microstructure. Conversely, the data were also collected into 10 vertical strips in order to check particle site uniformity across the stringer direction. The findings of this analysis for the two microstructures in Figure 5 are summarized below in Table 3.

The results are conveniently evaluated by means of the R-parameter, which merely expresses the degree of divergency or fit of the experimental data referred to a theoretical uniform distribution with expected value E. This distribution appears to represent physically the attributes expected of a "random" distribution of particles in a plane, and compares favorably with results obtained with a Poisson distribution or one obtained from random number tables.

It can be seen in Table 3 that the particle locations measured with horizontal strips diverge strongly from the theoretical uniform distribution (R = 4.6 and 3.2).

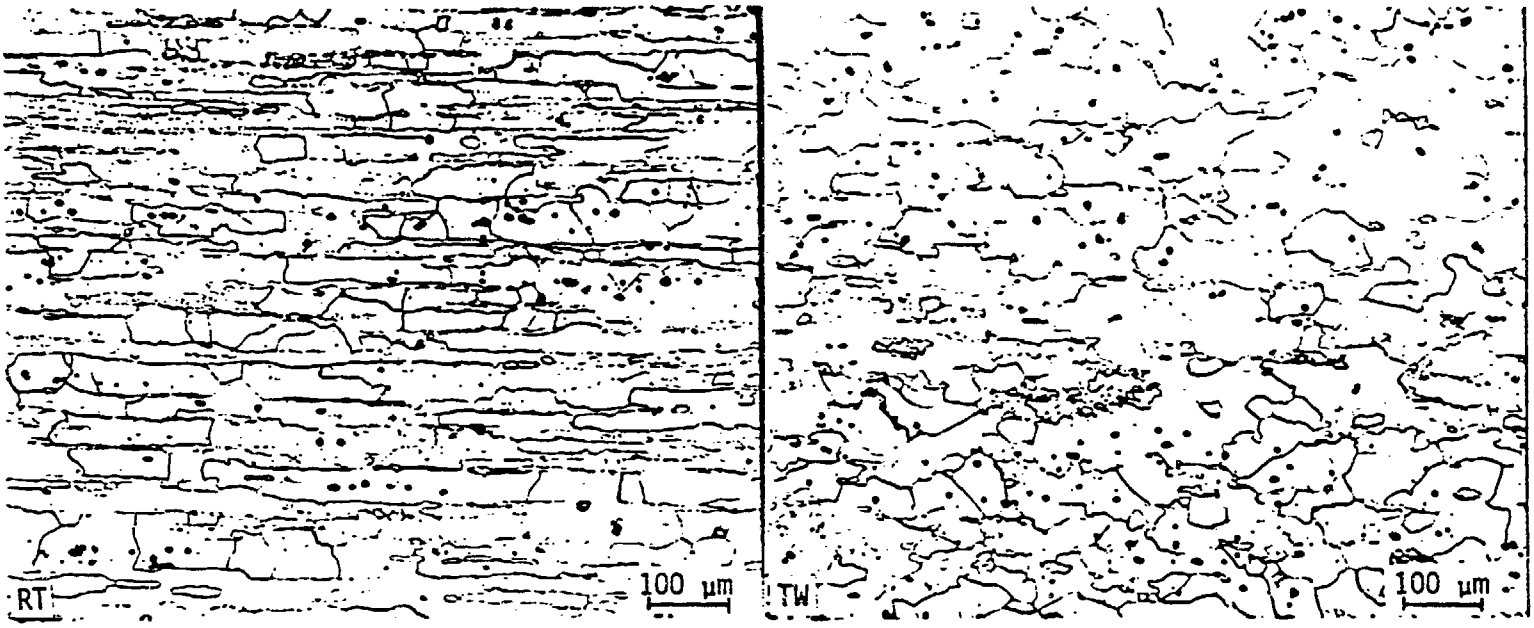


FIG. 5-Microstructure of longitudinal (RT) and transverse (TW) sections of ITMT processed 7050-T6X1 plate. Keller's etch.

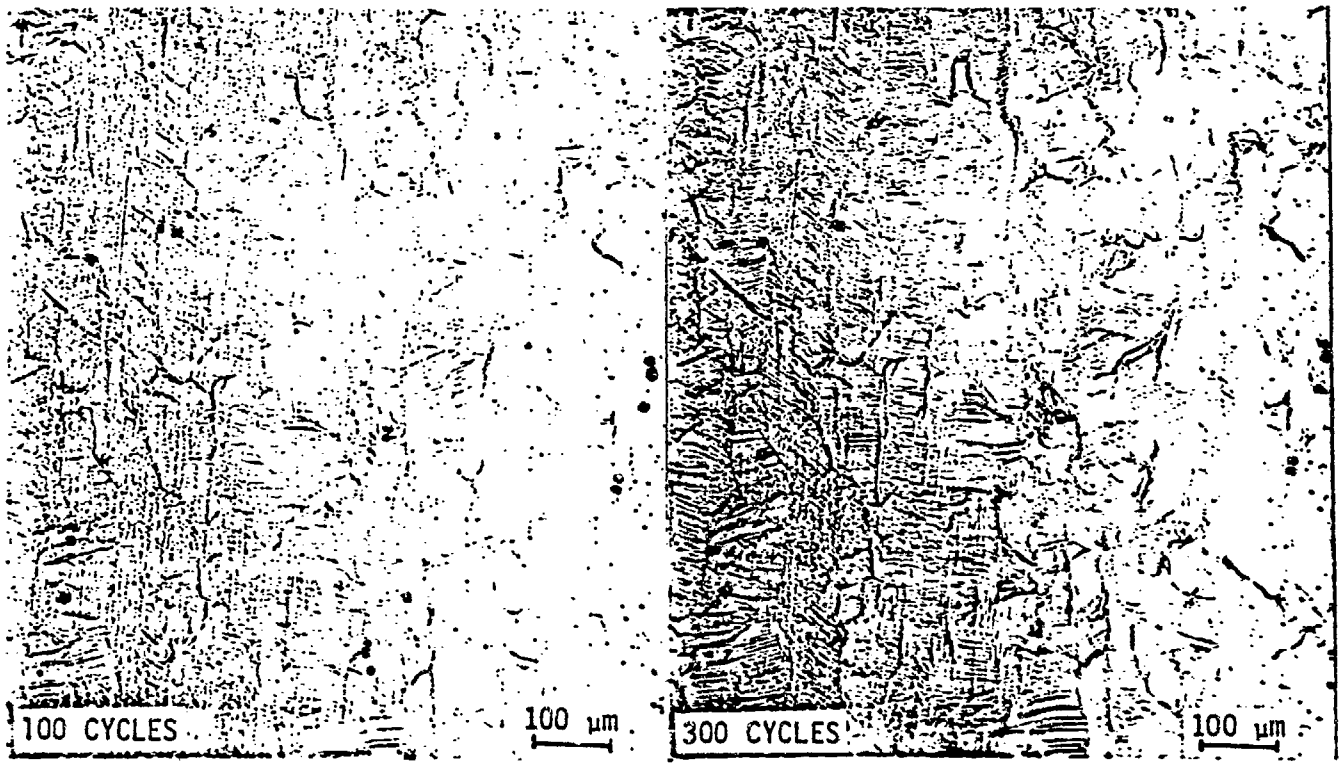


FIG. 6-Light micrographs of a tension-compression low-cycle fatigue sample of commercially processed 7050-T6X1. Stress axis vertical, $\Delta\varepsilon_T/2 = 1.2\%$. Unetched.

TABLE 3-Analysis of locational randomness of particles in Figure 5.

| Specimen | Total No. of Particles | Horizontal Rows (8)[a] | | | Vertical Columns (10)[b] | | |
|---|---|---|---|---|---|---|---|
| | | E | $\chi^2_{meas}$ | R | E | $\chi^2_{meas}$ | R |
| RT | 195 | 24.4 | 57.9 | 4.6 | 19.5 | 11.2 | 0.7 |
| TW | 247 | 30.9 | 40.0 | 3.2 | 24.7 | 16.6 | 1.1 |

a. $\nu = 6$, $p = 0.05$, $\chi^2_{th} = 12.59$

b. $\nu = 8$, $p = 0.05$, $\chi^2_{th} = 15.5$

$\nu$ is the degree of freedom, p the probability, and $\chi^2_{th}$ is the theoretical (tabular) value of chi-square. E is the expected value and R is the ratio $\chi^2_{meas}/\chi^2_{th}$.

However, the particle locations measured by vertical strips are quite uniformly distributed (R = 0.7 and 1.3). This type of analysis appears to possess considerable practical utility in addition to simplicity of calculation. Moreover, with good particle contrast, the strip counting technique may be performed readily by automatic image analysis.

The same RT specimen which provided Figure 5 was analyzed on the Bausch and Lomb FAS for particle heterogeneity. The variable frame control reduced the measured field on the TV screen to a narrow strip parallel to the particle stringers. Particle densities were measured within the strip at each of 12 successive locations. The results of the calculations are summarized as follows: $\chi^2_{meas} = 59.71$; $\chi^2_{th} = 18.31$, R = 3.3. Considering that a different field of view was analyzed here than the one shown in Figure 5 (RT-plane), the agreement is considered excellent.

## CRACK INITIATION SITES AND PARTICLE INTERACTIONS

Microstructure control through modification of conventional processing methods has recently been examined as a way of upgrading the fatigue resistance of 7XXX alloys.[5] A commercially processed (CP) 7050-T6X1 alloy, with a partially recrystallized structure ( ~50%) and an intermediate thermomechanically processed (ITMT) 7050-T6X1 alloy, with a fine, equiaxed, recrystallized grain structure, have been chosen for analysis. Micrographs were prepared from tension-compression low cycle fatigue samples, $\Delta\varepsilon_T/2 = 1.2\%$, at 100 cycles and at 300 cycles from the pre-polished and unetched surfaces.

Several basic stereological measurements were performed on both alloys. With respect to the cracks observed at the various sites, four quantities are of interest. They are $L_A$, the total length of crack traces per unit test area; $N_A$, the number of crack initiation sites per unit test area; $\bar{L}$, the mean crack length; and $\Omega_{12}$, the degree of orientation of the crack traces with respect to the direction normal to the stress axis.

The applicable equation for total crack length per unit area is

$$L_A = \left(\frac{\pi}{2}\right) P_L \tag{13}$$

where $P_L$ is the number of crack traces intersected by unit length of a test grid. In this case, a grid of 38 X 38 lines with ½-cm spacing was applied to the micrographs in Figures 6 and 7. For the CP alloy at 100 cycles, the number of intersections P = 164. The test length, $L_T$, when corrected for magnification, is equal to 7.16 cm. Thus $P_L$ (= $P/L_T$) = 164/7.16 = 22.91 $cm^{-1}$, and $L_A$ = 35.99 $cm^{-1}$. The

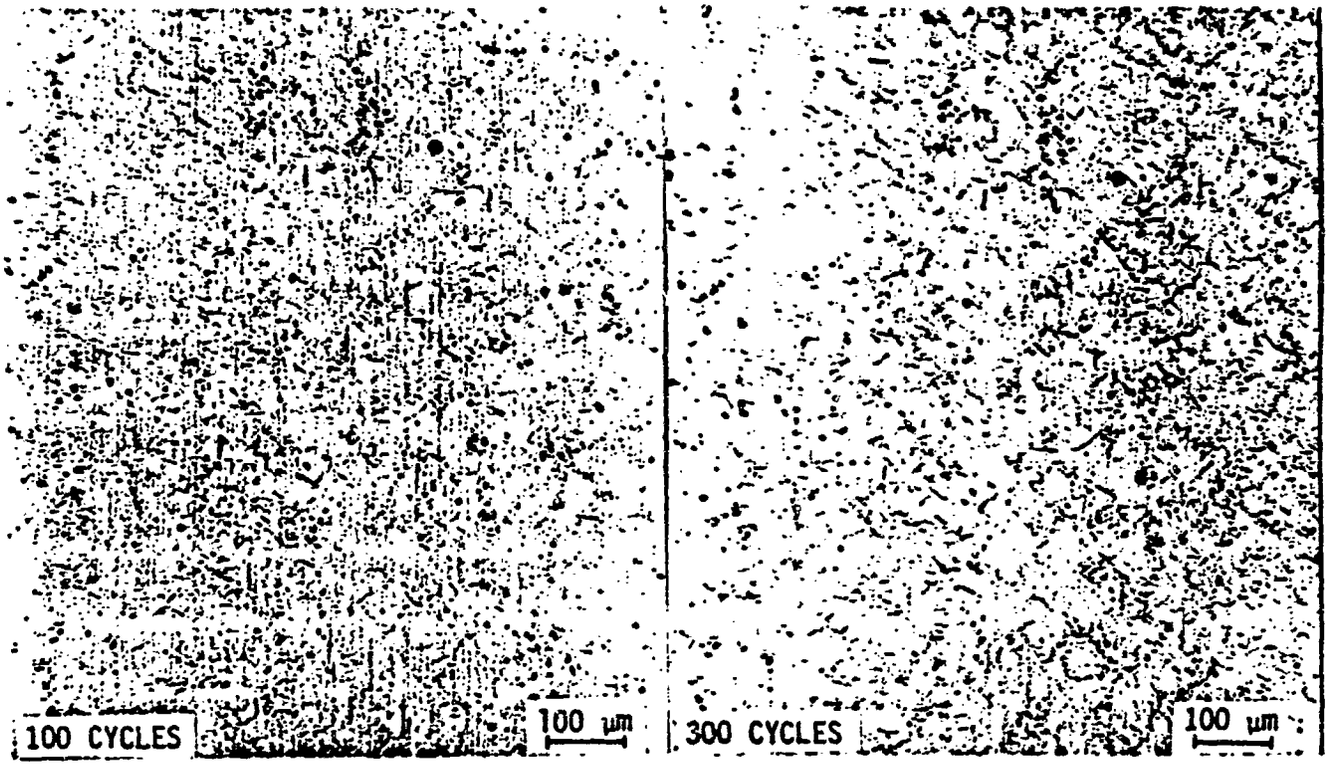


FIG. 7-Light micrographs of a tension-compression low-cycle fatigue sample of ITMT processed 7050-T6X1. Stress axis vertical, $\Delta\varepsilon_T/2 = 1.2\%$. Unetched

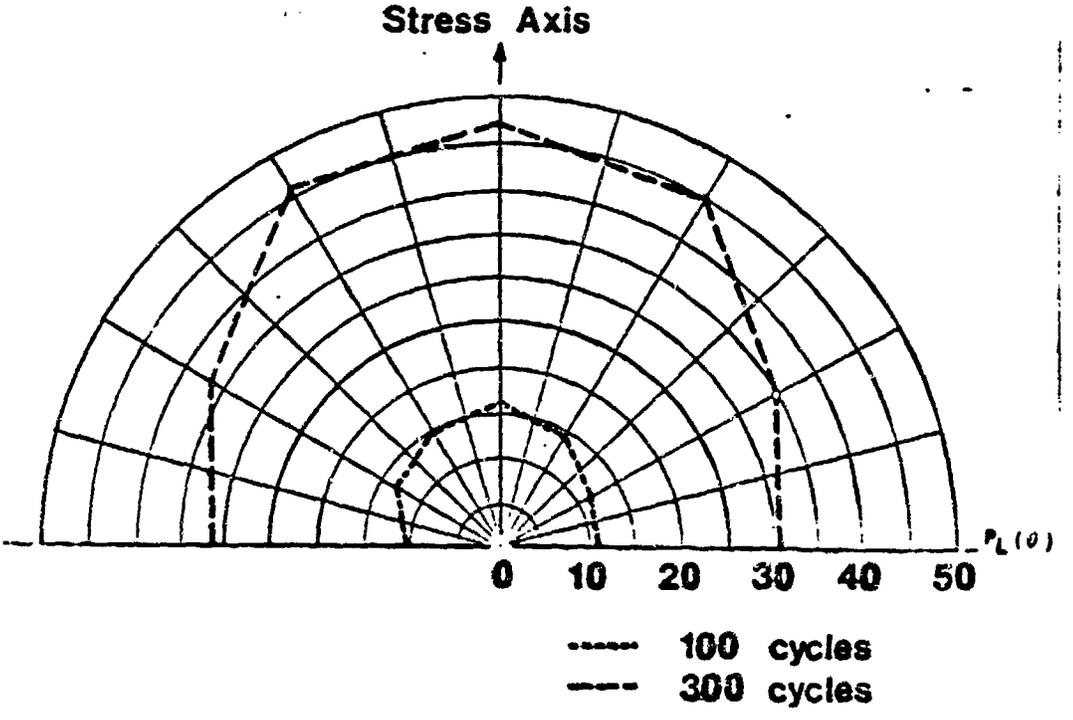


FIG. 8-Distribution of crack traces represented as density of intersections $P_L(\theta)$ versus angle $\theta$ for the LCF sample of ITMT-7050 shown in FIG. 7.

next quantity, $N_A$ (= $N/A_T$), for the same alloy and condition, is obtained by a count of separate cracks, giving N = 84. The number of cracks per unit area, $N_A$, then equals $\frac{84}{19 \times 24/250^2}$ or 11,513 $cm^{-2}$, since the linear magnification is 250X. The mean crack length, $\bar{L}$, is equal to $L_A/N_A$. In this case $\bar{L}$ = 35.99/11,513, giving a value of 31.3 μm. The fourth parameter calculated here is $\Omega_{12}$, the degree of orientation for lines in a plane, which is defined in Eq. 10. It has the value of 0 for a set of lines with completely random orientations, and value of unity for a set of lines completely parallel to the orientation direction. Since the cracks tend to lie normal to the stress axis, the normal direction is chosen for the orientation axis, thus $\perp$ and $//$ refer to measurement directions of the grid perpendicular and parallel, respectively, to the chosen orientation axis. In this case, we find that $(P_L)_\perp$ = 24.58 $cm^{-1}$ and $(P_L)_{//}$ = 21.23 $cm^{-1}$, giving a value for $\Omega_{12}$ of 9.13 percent. These four basic quantities are tabulated in Table 4 for each of the four alloy conditions shown in Figures 6 and 7.

Note that the crack orientations in the CP alloy are almost random--only 9 percent of the linear elements is aligned parallel to the orientation axis. In the ITMT alloy, however, we see that about one-fourth of the total crack trace length is oriented normal to the stress axis. It is also noteworthy that the degree of orientation for both alloys does not change significantly between 100 and 300 cycles, even though the total crack length increases by a factor greater than three.

Etched specimens of CP and ITMT alloys show that the grain size is much finer and more uniform in ITMT than CP. Moreover, coarse slip bands appear only in the CP alloy. These factors may account for the 50 percent greater mean crack length in the CP alloy. The stronger, finer grain size ITMT alloy also has less crack nuclei. The grain shape in ITMT is quite equiaxed and the alloy is completely recrystallized, while the CP alloy is only partially recrystallized and the grains are relatively large and elongated along the stress axis. Thus the ITMT grain boundaries are more randomly oriented, providing more boundaries at $90^0$ to the stress axis for crack nuclei, as reflected in the higher values of $\Omega_{12}$.

It may be significant that the number of crack initiation sites are greater in the CP alloy, even though there are fewer grains per unit area. Moreover, it appears that numerous crack nuclei have originated at slip band traces, which would account for the lower degree of orientation in the CP alloy. It should be noted that grain size, grain shape, and length and orientation of the slip band

TABLE 4-Basic microstructural crack parameters for CP and ITMT processed 7050 after fatigue testing for 100 and 300 cycles.

| | CP-7050 | | ITMT-7050 | |
|---|---|---|---|---|
| Parameter | 100 cycles | 300 cycles | 100 cycles | 300 cycles |
| $L_A$, $cm^{-1}$ | 35.99 | 108.82 | 19.45 | 63.34 |
| $N_A$, $cm^{-2}$ | 11,513 | 32,740 | 9,589 | 26,849 |
| $\bar{L}$, μm | 31.3 | 33.2 | 20.3 | 23.6 |
| $\Omega_{12}$, % | 9.13 | 9.06 | 27.4 | 24.8 |

traces can also be determined quantitatively, and the techniques for doing this have been described elsewhere in this paper.

Additional information on the angular distribution of crack traces is provided by the rose-of-the-number-of-intersections (called the "rose", for short). This is a polar plot that graphically portrays the density of intersections $P_L(\theta)$ of crack traces with the test lines, as a function of angle $\theta$, with respect to the orientation axis. Figure 8 gives the rose plot for the ITMT alloy after 100 and 300 cycles. From the characteristics of these curves, it can be deduced that the angular distribution of crack traces belongs to the classification "Partially-oriented system of lines in a plane". It is also of interest that the degree of orientation ($\Omega_{12}$) of both curves is essentially the same, even though $P_L$ at 300 cycles is more than three times greater than at 100 cycles. The rose shows us that the value of $P_L(\theta)$ proceeds smoothly from a minimum value at $\theta = 0^o$ to a maximum value of $P_L(\theta)$ at $\theta = 90^o$. This implies that the crack sites are probably located at the randomly-oriented grain boundaries. The evidence in Figure 7, as well as in etched photomicrographs, appears to confirm this suggestion qualitatively.

The possible role of particles on the crack site initiation behavior can be investigated by a statistical technique. The relatively large particles in Figure 7 are disposed more in vertical columns than randomly. Some particles are associated with crack sites, but many are not. In order to assess the degree of positional randomness, their locations are compared with those of a hypothetical uniform distribution, and evaluated numerically by the $\chi^2$ test for goodness of fit as described above. The experimental details are somewhat different. Here we use 9 vertical columns and 11 horizontal rows to analyze the particle locations. The results of this analysis for the ITMT alloy after 300 cycles are summarized below in Table 5.

It can be seen immediately that the particle locations as measured with vertical strips diverge strongly from the theoretical uniform distribution, and this is reflected by a $\chi^2_{vert}$ almost 4 times greater than $\chi^2_{th}$. However, the particle locations measured by horizontal strips are quite uniformly distributed (R = 1.08). The same conclusion is reached for the crack site distributions. Both the vertical and horizontal cell analyses yield R values less than unity (R = 0.92 and R = 0.80), which would indicate excellent uniformity of location of the crack sites. As a conclusion, we may state that the large, stringered particles in the ITMT alloy do not interact significantly with the random nucleation of crack sites.

A less elaborate analysis of particle interactions with crack sites is afforded by the CP alloy microstructure. Figure 6 reveals that particle size and volume

TABLE 5-Particle and crack site uniformity of location analysis.

| Particle Distribution (Total number counted = 844) | | Crack Site Distribution (Total number counted = 182) | |
|---|---|---|---|
| Vertical Cells (9) | Horizontal Cells (11) | Vertical Cells (9) | Horizontal Cells (11) |
| $\chi^2_{vert} = 55.67$ | $\chi^2_{hor} = 18.21$ | $\chi^2_{vert} = 13.00$ | $\chi^2_{hor} = 13.60$ |
| $\chi^2_{th} = 14.067$ | $\chi^2_{th} = 16.919$ | $\chi^2_{th} = 14.067$ | $\chi^2_{th} = 16.919$ |
| R = 3.96 | R = 1.08 | R = 0.92 | R = 0.80 |

fraction are significantly less than in the ITMT alloy (Figure 7). However, a close inspection of Figure 6 shows that a large number of crack sites are associated with small particles. In fact, only 18 out of 84 crack sites do not appear to have particles present, and many of those without particles appear to originate at slip band traces. Thus there seems to be a critical particle size effect, such that below a certain size, particles interact significantly with crack nucleation. At larger particle sizes, the effect appears to be lost.

## CRACK INTERACTIONS

Conventionally, crack lengths in fatigued specimens are monitored along the specimen surface by optical comparators or ultrasonic probes. Metallographic specimens usually show only the two dimensional trace of the crack, edge-on and parallel to the CGD. The length measured actually corresponds to the projected length (from initial point to the crack tip) and not to the true length of the meandering crack. Moreover, for some purposes, it is the true crack surface area that is required, rather than the simple linear quantity.

Within these qualifications, there are still several important features of the crack--its own characteristics and the interactive aspects--that require quantification. Among these more important features are the extent of transgranular vs. intergranular path length; the "true" crack length vs. the projected crack length; the extent of branching; and the actual crack surface area. Interactions of cracks with grains and sub-grains, with particles, recrystallized regions, and slip band traces are also important. The methods of quantification, both generally and for special cases, are discussed for several specific microstructures.

Figure 9 represents a typical branched fatigue crack in an underaged (4 hr at 120°C) Al-Zn-Mg-(Zr) alloy, compact tension specimen, $\Delta K = 10$ MPm$^{-\frac{1}{2}}$. The first item of interest is the conventional crack length, or the length from initial point to the crack tip, measured in a direction parallel to the main crack growth direction. This distance, the projected length, is $L_{proj} = 0.025$ cm. In contrast, the total true crack length $L_t$ consists of all linear elements of the crack traces, whether belonging to the main branch, sub-branches, or disconnected segments. The total true crack (trace) length per unit area is simply $L_A$ or $L_t/A_T$ where $A_T$ is the test area. Since $L_A = (\frac{\pi}{2}) P_L$, the absolute value of length is:

$$L_t = (\tfrac{\pi}{2}) P_L A_T \qquad (14)$$


FIG. 9-Light micrograph illustrating crack path of an underaged (4 h at 120°C) Al-6Zn-2Mg-0.11Zr alloy. Compact tension sample, laboratory air, $\Delta K$ = 10 $MPm^{-\frac{1}{2}}$. Keller's etch.

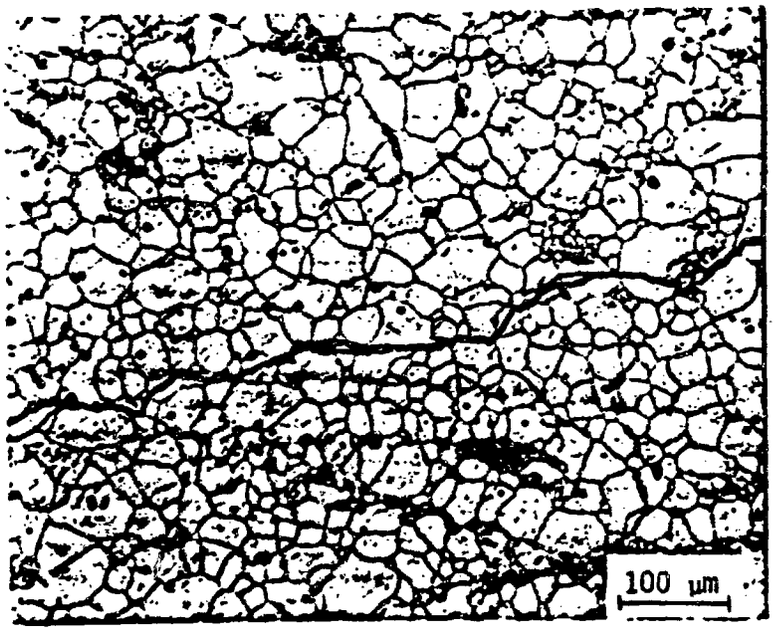


FIG. 10-Light micrograph illustrating crack path of an ITMT-7050-T6X1 alloy. Compact tension sample, dry $N_2$, $\Delta K$ = 8 $MPm^{-\frac{1}{2}}$. Etched in 25% $HNO_3$ at 70°C.

and $P_L$ is the number of points of intersection of crack traces with the test lines, applied at many angles, per unit length. In order to avoid some subtle problems, it is generally advisable to clearly define a convenient test area, then apply a test grid of parallel lines that covers the entire test area from all angles. The test line length in this case is considered to be the same regardless of angle of placement.

Based on the procedure outlined above, $L_t$ for the total crack length is obtained from Eq. (14) according to:

$$L_t = \left(\frac{\pi}{2}\right) 70.6\ (9.10^{-4}) = 0.0998 \text{ cm.}$$

Intersection measurements on the main crack trace give a value of only $L_t = 0.0272$ cm. Thus, we have in summary:

| | |
|---|---|
| Total crack length: | $L_t = 0.0998$ cm |
| Main crack length: | $L_t = 0.0272$ cm |
| Projected length: | $L_{proj} = 0.025$ cm |

Some significant crack length ratios are:

$$\frac{(L_t)_{total}}{L_{proj}} = 3.99$$

$$\frac{(L_t)_{total}}{(L_t)_{main\ crack}} = 3.67$$

$$\frac{(L_t)_{main\ crack}}{L_{proj}} = 1.09$$

It is important that these typical characteristics of fatigue cracks be considered in the detailed analysis of the crack growth process.

In addition to crack length studies, the degree of orientation $\Omega_{12}$ for branched cracks is also pertinent to macroscopic crack growth measurements. Based on simple measurements of $(P_L)_\perp$ and $(P_L)_\parallel$, Equation (10) yields a value of $\Omega_{12} = 17.5\%$. This is a rather small percentage of total crack length to be oriented in the crack growth direction.

A final consideration here is the general problem of expressing crack length in terms of the actual crack surface area. When estimating the energy of forming a crack, for example, a parameter of interest is surely the true crack area. Two situations can be handled quantitatively from the usual crack trace on polished specimen surface. For randomly oriented crack surface elements, we invoke the general equation

$$S_V = \left(\frac{4}{\pi}\right) L_A \tag{15}$$

between crack surface area per unit volume and crack trace length per unit area. Serial sectioning may be necessary to improve the accuracy of the results. On the other hand, when crack surface elements are all normal to the plane of the crack trace, then another equation applies. It is

$$(S_V)_\perp = L_A \tag{16}$$

which states simply that the area per unit volume of crack surfaces perpendicular to the crack trace plane is equal directly to the length of crack trace per unit area on that plane. The magnitude of the difference between these two extremes is calculated for the main crack. For random crack surfaces we have $S_V = (4/\pi)\ L_A = 2\ P_L = 2\ (29.17) = 58.3\ cm^{-1}$; for oriented crack surfaces normal to the crack trace plane, we find $(S_V)_\perp = L_A = (\pi/2)\ P_L = 1.571\ (29.17) = 45.8\ cm^{-1}$. Thus in the limit there can be a 27 percent increase in crack surface area between an oriented and a random crack surface. Generally, the true state of affairs can be expected to lie somewhere between these two extremes. As the crack surface tends more toward flatness, the coefficient between $L_A$ and $S_V$ will move closer to unity.

An analysis of the fatigue crack path through recrystallized grains of ITNT-7050-T6X1 alloy was also undertaken. Figure 10 shows a crack that has progressed from left to right, across grains and through grain boundaries. In order to determine the extent of transgranular crack path vs. the amount of intergranular fracture, a random $P_L$ intersection count was performed. Intersections of a randomly-applied linear test grid with transgranular crack elements gave $P_{trans} = 24$, and for intergranular crack elements, $P_{inter} = 14$. Equation (14), $L_t = (\pi/2)\ P_L\ A_T$, gives the following results:

$$L_{trans} = 1.571\ (14.0)\ 1.84 \cdot 10^{-3} = 40.5 \cdot 10^{-3}\ cm$$
$$L_{inter} = 1.571\ (8.17)\ 1.84 \cdot 10^{-3} = 23.6 \cdot 10^{-3}\ cm$$
$$L_{total} = 1.571\ (22.17)\ 1.84 \cdot 10^{-3} = 64.1 \cdot 10^{-3}\ cm$$

Ratios of these quantities show that

$$\frac{L_{trans}}{L_{inter}} = \frac{P_{trans}}{P_{inter}} = \frac{24}{14} = 1.7$$

and

$$\frac{L_{trans}}{L_{total}} = \frac{P_{trans}}{P_{total}} = \frac{24}{38} = 0.63 = (\iota_t)_{trans}.$$

Thus it is seen that the crack definitely favors the transgranular path. The ratio $(\ell_\ell)_{trans} = 0.63$ is the lineal fraction of transgranular crack length along the crack path; as such, it is not the same as the lineal fraction $L_L$ obtained with straight test lines over the microstructure. Crack interaction with particles appear negligible, although particles on the fracture surface were noticeable. A count was also made of the grains in Fig. 10 that were cut transversely or intergranularly by the crack path. The numbers obtained, $N_{trans} = 20$ and $N_{inter} = 15$, yield a ration $N_{trans}/N_{inter} = 1.33$ which compares roughly with $L_{trans}/L_{inter} = 1.7$. A simple count may suffice for some purposes when more elaborate procedures are not justified. The grain size was measured in a direction parallel to the crack path. The mean intercept length $\bar{L}_{//} = 20$ μm.

Cracking is seen to occur through subgrains in an Al-Zn-Mg-Cu alloy, in Figure 11. The crack path runs parallel to a layer of coarse recrystallized grains, and except for a few larger subgrains or grains, the crack follows a mostly intersubgranular path; i.e., $L_{inter}/L_{total} = 0.61$. The ratio of $L_{inter}/L_{trans} = 1.55$ compares well to the grain count ratio $N_{inter}/N_{trans} = 1.62$ in these very fine subgrains ($\bar{L}_{//} = 2$ μm).

A TEM of the subgrains in the same alloy is shown in Figure 12. The low-angle boundaries are heavily populated with η' precipitates which are believed to be partially responsible for the crack preference for subgrain boundaries. A brief analysis is made later of precipitates at boundaries as measured from thin foil photomicrographs.

Cracking at particles is also a common occurrence in fatigued specimens. Figure 13 shows a cluster of particles in a fatigued ITNT-7475-T6 alloy. Several features of interest are observed, such as cracked particles, voids, debonding and crack nuclei at the particle interface. Voids can be measured by a point count ($P_p = V_v$); particle crack length by an intersection count ($L_A = (\pi/2)\, P_L$); interfacial length where debonding occurs (also by $L_A$); and void-particle proximity can be evaluated by the contiguity parameter (see Eqs. 11 and 12).

The particle projected length with respect to a chosen projection line has been used in studies of fatigue-particle interactions.[6] This projected length L' may be measured readily in an automatic image analysis system for each particle in a field of view. This would be laborious if done manually. However, if the mean tangent diameter $\bar{d}$ (i.e., the mean of the projected lengths) is acceptable, it is obtained readily on the plane of polish by

$$\bar{d} = \frac{N_L}{N_A} \qquad (17)$$

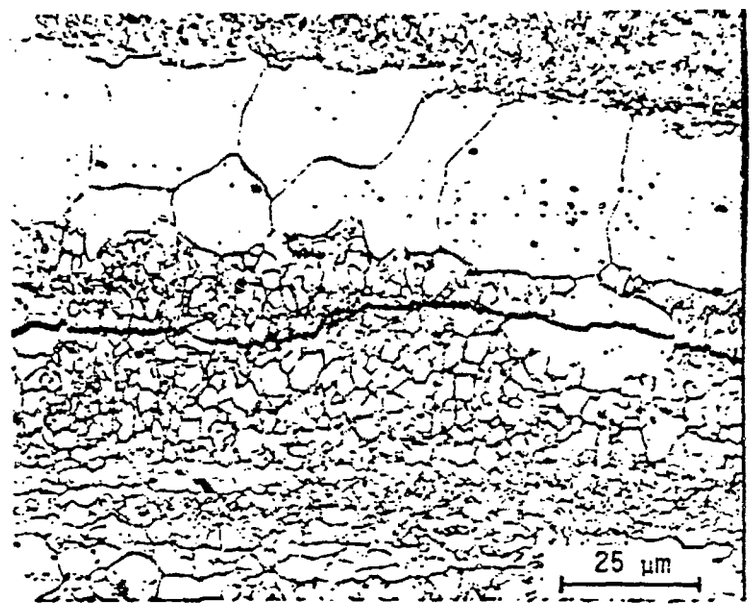


FIG. 11-Light micrograph illustrating crack path in subgrains of unrecrystallized region of an Al-6Zn-2Mg-2Cu-0.12Zr alloy aged 24 h at 120°C. Compact tension sample, distilled $H_2O$, $\Delta K = 6\ MPm^{\frac{1}{2}}$. Etched in 25% $HNO_3$ at 70°C.

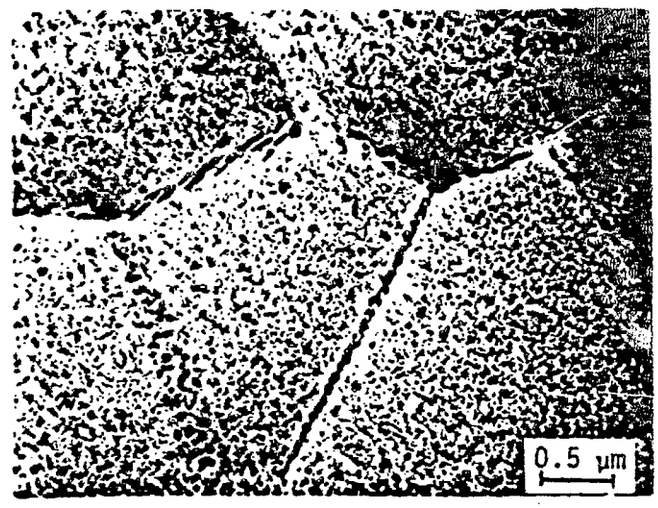


FIG. 12-Transmission electron micrograph of an undeformed section of the sample shown in FIG. 11 illustrating precipitates along subgrain boundaries of unrecrystallized grains.

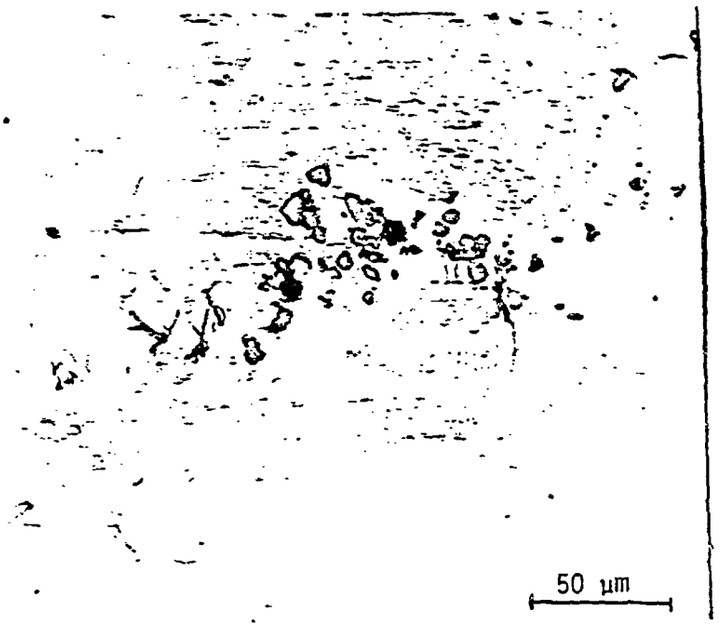


FIG. 13-Light micrograph of an ITMT-7475-T6 LCF sample showing cracked particles and small fatigue cracks. Stress axis horizontal. Unetched.

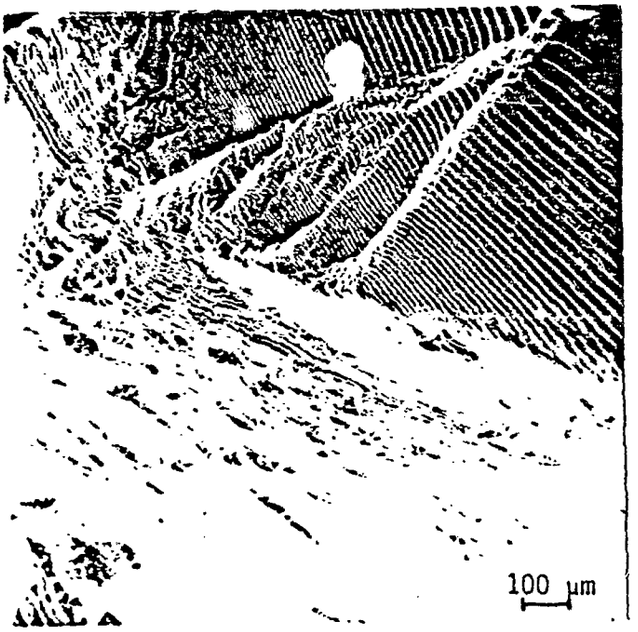


FIG. 14-Scanning electron micrograph of a disordered $Cu_3Au$ single crystal LCF sample. $\Delta\epsilon_T/2 = 0.85\%$, $N_f = 1{,}800$ cycles.

where $N_L$ is the number of particles intercepted per unit length of test line and $N_A$ is the number of particles per unit test area. Moreover, the mean projected length, in one direction, for a system of particles is given by

$$\bar{L}' = \left(\frac{L_L'}{N_L'}\right)_{\perp} = \left(\frac{P_P'}{N_L'}\right)_{\perp} \tag{18}$$

where the primes indicate that these are measurements made on the projection line, and the $\perp$ indicates that the direction of the test lines are perpendicular to the projection line. Further details of the possibilities here can be found in the treatments of projections in a plane to a projection line.

FATIGUE STRIATIONS

Microscopic features of the fracture surface have been correlated many times with macroscopically measured crack growth rates in mechanistic studies of fatigue crack propagation. One such feature, fatigue striation spacing, is associated with local crack growths rates which may or may not be different from the macroscopically measured values. Theoretically calculated crack growth rates should be correlated with the striation spacing measured on the fracture plane in the local growth direction. This is, of course, only true when the striation mode of crack propagation controls the fatigue crack growth. For mixed mode crack propagation, the amount of each mode must be assessed quantitatively for accurate theoretical analysis.

There are at least two general problems underlying the measurement of fatigue striation spacings (FSS). First the normals to the striations do not always lie in the crack direction; and secondly, the striations usually occur on fracture surfaces that are decidedly non-planar. Figure 14 represents a typical fracture surface with striated facets oriented at many angles.[7] Four types of striated fracture surfaces are of interest to this study. Figure 15 illustrates their important characteristics as they would appear in a TEM photomicrograph.

Most microscopic analysis is done on flat photomicrographs or images of the fracture surface, such as obtained from replicas by TEM or scanning electron microscopy (SEM). Thus we are dealing with projected images, and the stereological relationships applicable to this situation must be invoked in order to extract as much quantitative information from the projection plane as possible.[1,8]

For example, the striations in Figure 15(a) cover the sampled fracture surface completely. The FSS are quite uniform, and the striation directions (their normals)

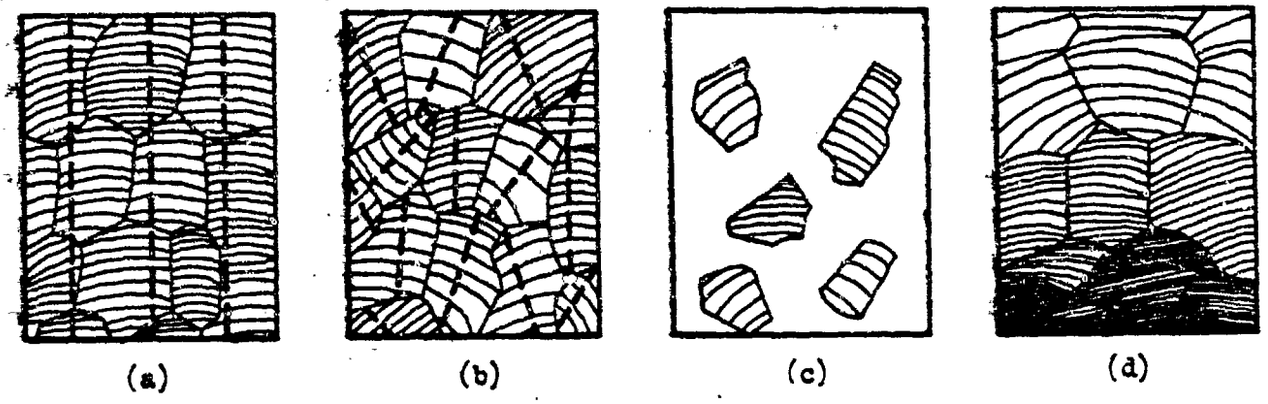


FIG. 15-Typical types of striated fracture surfaces; crack growth direction vertical. (a) Uniformly-oriented striations; (b) randomly-oriented striations; (c) partial coverage by striations; and (d) gradient of striation spacing.

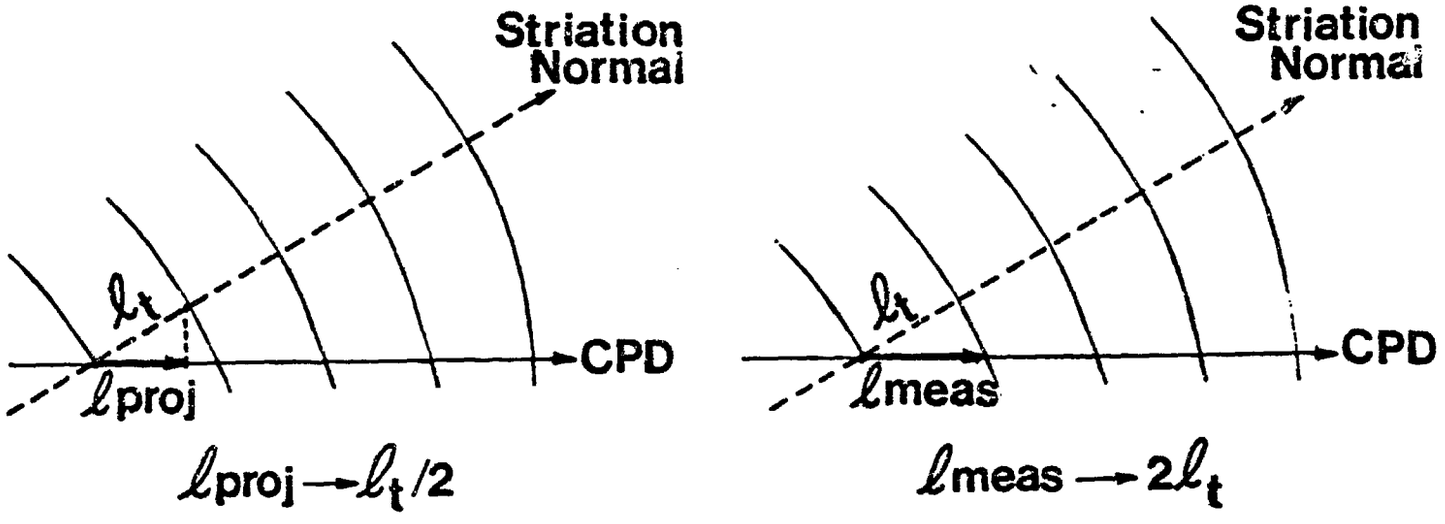


FIG. 16-Geometry involved in two different techniques for striation spacing measurement.

are all fairly close to the crack propagation direction (CPD). In Figure 15(b), the major difference is that the striation-facet directions are oriented differently with respect to the CPD. The striated facets in Figure 15(c) are much the same as in Figure 15(a) or (b), but do not cover the fracture surface completely. This situation obscures the direct FSS relationships found in the literature[9] because of the mixed mode of fracture. In Figure 15(d), we see striations covering the sample completely, but there is a definite gradient of spacings along the CPD. In order to analyze these four prototype microstructures quantitatively, somewhat different measurement techniques should be employed. The details will be presented later, after discussing the advantages and disadvantages of different types of measurements.

Generally, the number (N) of striations intercepting a straight line (of length L') is counted on a planar photomicrograph, giving the apparent mean center-to-center spacing (L'/N) between adjacent striations. The primes indicate quantities in the projection plane, in order to distinguish them from the true microstructural quantities. In one measurement method,[10] the FSS in each striation facet is measured in a direction normal to the striation lines, regardless of the CPD. The various values of FSS are then recalculated by projecting to a line parallel to the CPD. The corrected values are then averaged. This method is quite laborious and time-consuming if done manually, and considerable calculation is involved. However, some automatic image analysis systems can measure spacings within localized regions.[11]

In a second method,[12] a straight test line (or better, a grid of parallel test lines) is laid down on the photomicrograph parallel to the CPD. The interceptions are then counted, regardless of striation orientation, and the total number of interceptions divided by the total length of grid lines to give the average apparent striation spacing. This method is appreciably faster than the first method described above.

It should be noted, however, that the first method gives a value of FSS <u>smaller</u> than the "true" normal spacing, while the second method <u>over-estimates</u> the "true" normal spacing. The sketches in Figure 16 give the essential geometrical relationships. Note that in one case, the spacing employed ($\ell_{proj}$) approaches one-half the value of the apparent true spacing ($\ell_t$), while in the other, the measured spacing ($L_{meas}$) approaches <u>twice</u> the value of $\ell_t$. The two relationships become exact when all possible angles between striation normal and CPD are present.

In addition to the above, there is an error in the measurements of FSS due to the non-planar character of the fracture surface. In general, the striation spacings measured from the photomicrograph will be too small. Figure 17 sketches the elements of the structure as viewed in a vertical section through the fracture surface and parallel to the CPD. It can be seen that the measured spacing (L'/N) is not the true spacing ($L_t$/N), because L', the projected test line length is less that $L_t$, the true length of test line.

Several techniques are available for estimating the true length of test line in the fracture surface, none of which are very satisfactory at the present time. A rather laborious procedure is to mount the specimen, make vertical sections through the fracture surface parallel to the overall CGD, and measure the true length $L_t$ on each section. The appropriate equation in this case is Eq. 14 where $A_T$ is the selected test area enclosing the fracture surface profile. Having obtained the value of $L_t$ (or an average value) we can apply the correction factor ($L_t$/L') as indicated by

$$\ell_t = \left(\frac{L'}{N}\right)\left(\frac{L_t}{L'}\right) \qquad (19)$$

Note that Eq. 19 corrects only for lack of planarity of the fracture surface.

Some experimental data are available on the magnitude of the ratio $L_t$/L'. Pickens and Gurland[13] measured this ratio for Charpy fracture surfaces in SAE 4620 steel and got values between 2.08 and 2.54, with the average equal to 2.32. The theoretical relationship between $L_t$ and L' is given by $L_t = \left(\frac{\pi}{2}\right) L'$ for a line in a plane randomly projected over all angles to a projection line. Thus, the coefficient $\pi/2$ is about 1.5 times smaller than the above experimental value of 2.32. This discrepancy is understandable, however, because the linear segments of $L_t$ do not lie randomly at all possible angles to the projection line, but instead are biassed preferentially with respect to the fracture plane (i.e., more are parallel to the projection line). Thus the observed coefficient is greater than the theoretical one, and a value of ($L_t$/L') = 2.3 does not appear unreasonable. Of course, for precise experimental research, the mean value of $L_t$/L' can be determined for the actual fracture surfaces being investigated. Several successive, parallel cuts (serial sectioning) through the fracture surface, as indicated above, give a mean value of correction factor that can be used with a greater degree of confidence for the specific material under study.

Returning now to Figure 15, we see that the measurement of striation spacings on the photomicrographs can be different in each case. The "best" method to

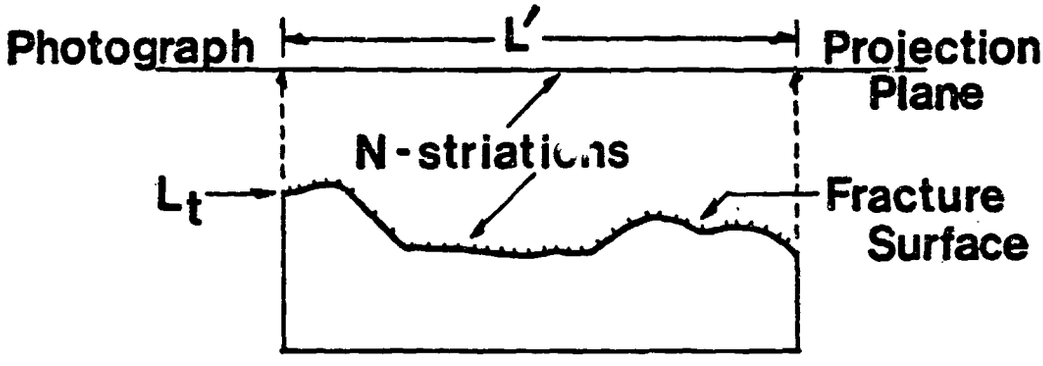


FIG. 17-Schematic of vertical section through fracture surface and parallel to crack direction.

use is probably that method which most satisfactorily fits the requirements of each job. For example, in Figure 15(a) the Second Method discussed above should prove adequate for most uniform, fairly well oriented structures. In Figure 15(b) however, where the striated regions are widely oriented with respect to the CPD, the First Method mentioned above may prove more useful. The availability of automatic image analysis instruments may also influence the choice of method selected. The problems associated with the structure shown in Figure 15(c) are not so much the measurement of striation spacings, as the determination of their direct applicability in view of the controlling mechanism of crack growth. However, if the area covered by striations represents the slower fracture mode, then the area fraction of striated regions maybe the required quantity. In Figure 15(d), where there is a local gradient of striation spacings, the simple average value may be satisfactory, or for more precise characterization, measurements of the spacings can be made at several locations along the gradient direction. On gradients that extend over the entire fracture surface, one technique is to measure the <u>average</u> local striation spacing at 5 or 6 locations, even though there may be a slight gradient within each sample.

A further caveat on the use of Eq. 14 should be noted. If measurements of $L_t$ are desired in order to calculate the true fracture surface area, then the type of fracture surface being sectioned must be known qualitatively. That is, for randomly-oriented surface elements in space, the applicable equation is Eq. 15, and for surfaces that are oriented <u>normal</u> to the vertical section, then use Eq. 16. Since most fracture surfaces will fall in between the two extremes of completely random and completely oriented (perpendicular to the vertical sectioning plane),the coefficient to use with $L_A$ will vary between unity and 0.7854. Inspection of the fracture surface with SEM should serve to guide the estimate of the coefficient to be used.

As a practical guide, it should be noted that even though Method 2 over-estimates the "true" normal spacing, the measurement of striations on the projection plane (instead of the true fracture surface) tends to underestimate the spacings. Thus, the errors involved are compensated to some extent. The magnitude of the errors have not been thoroughly investigated, but could be estimated by careful quantitative experimental work and statistical analysis.

## GRADIENT STRUCTURES

Although many microstructural features can be considered "random" in one way or another, there are other important classes of microstructures. We have dealt

previously with oriented structures, including layering of unrecrystallized lamellae, elongated grains, particle stringers, and striations--all as part of anisotropic structures. Another familiar type of microstructure belongs in the "gradient" classification, which may have point symmetry[14] or line symmetry[15] (in two- or three-dimensional space), planar symmetry, etc.

Two common types of gradient structures are discussed here. General treatments for representing a gradient quantitatively are unavailable, so methods must be devised for each particular case. Figure 18 shows the surface-to-center microstructure of an Al-6Zn-2Mg-2Cu-0.12Zr alloy that has been rolled down from 3.8 cm plate to 0.6 cm sheet. The dark lamellae are unrecrystallized layers, alternating with lighter etching recrystallized grains. The gradient effect, of course, arises from the smaller and smaller spacings as the center is approached. We treat this structure as an example of gradient symmetry in a plane about a centerline, although it actually has planar symmetry in three-dimensions.

A method was devised to extract some possibly useful information for the case of fatigue cracks progressing inward from the surface. A grid of parallel lines (set parallel to the surface edge) was placed on the microstructure from surface to centerline. Within each strip various quantities were measured, such as spacings, volume fractions, grain sizes, etc. This technique has the property that fine detail can be smeared out, or over-accentuated, depending on the width of the strip with respect to the microstructural detail. For this microstructure strips 0.1 mm wide were chosen, which subdivided the field of view into 40 strips.

To illustrate the type of data obtainable from a gradient structure, two plots are shown in Figure 18. The first gives the volume fractions ($L_L$) of unrecrystallized lamellae as a function of distance inward from the surface. A linear traverse was run down the middle of the microstructure normal to the lamellae. The fraction of unrecrystallized material traversed across each strip was recorded as $L_L$ and plotted as a function of distance from the surface. The bar graph portrays a gradual increase from zero lineal fraction at the surface to a maximum at the sheet center. A smoothed curve was faired in over the bar graph, based on the normal curve according to the equation $L_L = \frac{2.25}{\sqrt{2\pi}} \exp\left[\frac{-(x-3.4)^2}{2}\right]$, with x equal to the inward distance in mm. This, or some other suitable curve, can then be used to represent the gradient analytically.

The second curve in Figure 18 portrays the center-to-center lamellar spacing as a function of distance from the surface. The widest spacings occur about 1 mm under the surface, with a fall-off to either side. This information may be useful in qualitative form, or else could be expressed analytically, as desired.

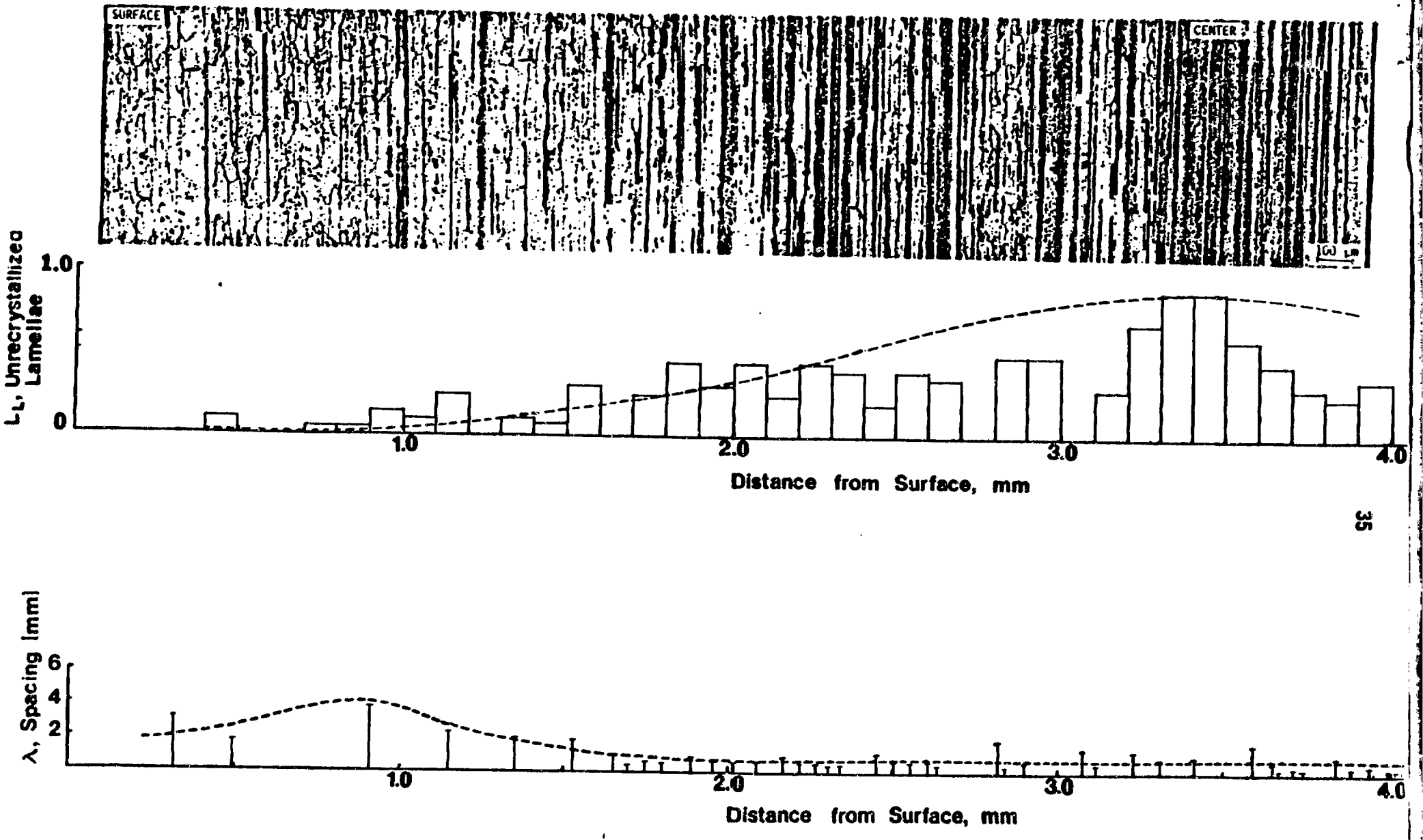


FIG. 18-Gradient grain structure of an Al-6Zn-2Mg-2Cu-0.12Zr sheet. Etched in 25% $HNO_3$ at 70°C.

Another example of a gradient structure is seen in Figure 19, which shows a single crystal of Cu fatigued to fracture.[16] The fatigue striation spacings increase smoothly from the origin to the outer surface of the specimen. The data collected here are analyzed in three ways. First the overall average striation density was found, i.e., 49 striations over a total diametral distance of 2.58 mm equals 18.99 $mm^{-1}$. Then the mean striation spacing was determined over intervals of $D_{max}/16$ and $D_{max}/8$ (i.e.,0.161 mm and 0.323 mm; respectively). The plotted bar graphs show the smallest interval to best advantage--the striation density increases smoothly to a maximum density near the origin, reaching 72.2 $mm^{-1}$. For the $D_{max}/8$ interval, however, the striation density is averaged out to a maximum density of only 46.5 $mm^{-1}$ near the origin. Thus, this simple analysis shows how the gradient data may be altered by the choice of interval. This is an important consideration and must be optimized for each case.

## THIN FOIL ANALYSIS

One of the most useful techniques available for revealing the fine structure of alloys is TEM from thin foils. Unfortunately, it is particularly difficult to get quantitative information from these projected images, primarily because of overlap and truncation problems. If foil thickness is small relative to particle diameter, however, overlap becomes less serious and useful estimates of volume fraction, particle size and particle density can be obtained.

Figure 20 shows a thin foil micrograph of an Al-0.5Fe-0.5Co wire, taken transversely to the wire axis.[17] Several important quantities have been calculated to illustrate the procedures involved. The number of $Al_6(Fe,Co)$ particles N' (= 84) and the projected test area $A'_T$ (= 9.92 $\mu m^2$) gives $N'_A$ = 8.47 $\mu m^{-2}$. A point count gave P' = 31 particles hit and $P'_T$ = 288 total test points applied, with $P'_P = A'_A$ = 0.108. The mean projected particle area $\bar{A}' = A'_A/N'_A$ = 0.0128 $\mu m^2$. Assuming spherical particles, the projected mean diameter $\bar{D}$ = 0.1277 μm. These results enable us to calculate the volume fraction, which is given by

$$V_V = -2\,\ell n(1-A'_A)\,\frac{D}{D+3t} = 0.0076 \qquad (20)$$

where $D = \bar{D}'$ and t = 2000 Å. This equation includes an overlap correction. The number of particles per unit volume $N_V$ was calculated four different ways[8] for comparison. The first expression is $N_V = N'_A/t$ giving $N_V$ = 43.4 $\mu m^{-3}$. No truncation or overlap of particles is assumed. The second relationship is $N_V = N'_A/(t+\bar{D}')$ = 25.9 $\mu m^{-3}$ and includes a truncation correction. The third and fourth equations do not allow for truncation or overlap effects, but do permit other experimental quantities to be used. They are $N_V = N'_L/\bar{D}'t$ = 32.7 $\mu m^{-3}$ and

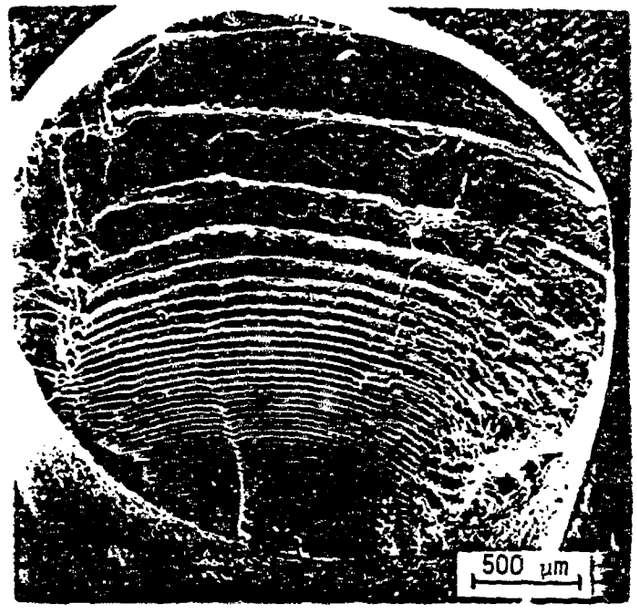


FIG. 19- Scanning electron micrograph of a Cu single crystal LCF sample. $\Delta\varepsilon_T/2 = 3.5\%$.

FIG. 20-Transmission electron micrograph of transverse section of Al-0.5Fe-0.5Co wire.

$N_V = P'_P/2t\bar{A}' = 21.1\ \mu m^{-3}$. The average value for all four calculations is $30.8\ \mu m^{-3}$. The results are considered to lie quite close together for an $N_V$ calculation.

A thin foil micrograph of ITMT - 7050-T6X1 is shown in Figure 21. The vertical grain boundary is heavily covered by η precipitates. Of interest is the precipitate density in the actual grain boundary. If we assume that the boundary is vertical, we can use the simple equation $N_S = N'_L/t$. With experimental values of $N' = 21$, $L'_T = 0.7\ \mu m$, $N'_L = 30\ \mu m^{-1}$ (along the boundary edge) and $t \approx 1000$ Å, $N_S = 30/0.1 = 300\ \mu m^{-2}$.

In cases where the boundary is inclined to the foil surface (as in Figure 12), the calculation of $N_S$ requires an estimate of the slant width from a knowledge of the foil thickness and the apparent boundary width, w'. Here we find that $N' = 155$ for the wide boundary at the lower left of the micrograph, and that $N'_A = 262.7\ \mu m^{-2}$. Correcting to true surface area using $t \approx 0.4\ \mu m$ and $w' = 0.3\ \mu m$, we get $S_{true} = 0.98\ \mu m^2$ and $N_S = 158.2\ \mu m^{-3}$. These are simple examples that do not reveal the complexities that arise in other thin foil structures. However, when simplifying assumptions are justified, fairly reasonable estimates can be obtained.

SYNOPSIS:

Several typical microstructural features which are important in fatigue studies have been selected to demonstrate the quantitative procedures of stereology. Both manual methods and automatic measurements (using the B&L Feature Analysis System) are employed, yielding excellent agreement in suitable structures. In a general treatment of microstructures with uniform grains and particles, we show how three simple counting measurements can yield most of the basic microstructural parameters. Next we deal with anisotropic materials and demonstrate the use of special methods suitable for this type of structure, such as the degree of orientation of surfaces and grain traces, average grain size, and directional spacings. The contiguity of particle interfaces is analyzed for a particular application in a three-constituent alloy.

Some localized microstructural features, especially particles, are very important to a process such as fatigue. A new statistical procedure has been developed for assessing the degree of locational randomness, or deviations therefrom, of particles in an alloy. A similar treatment is applied to the location of crack initiation sites in order to assess the interaction of particles and crack initiation sites. Prominent features of typical fatigue cracks are analyzed and

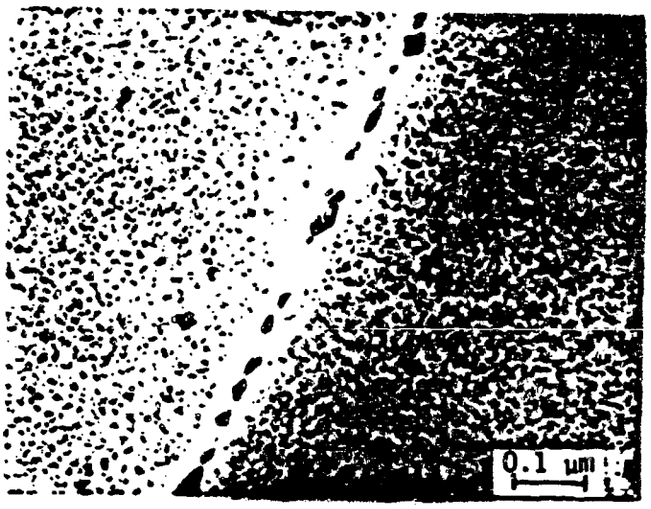


FIG. 21-Transmission electron micrograph of ITMT-7050-T6X1.

include true crack length, true crack surface area, and the quantitative evaluation of inter- and transgranular crack path lengths. A re-evaluation of methods for measuring striation spacings reveals possible sources of error, including errors arising from fracture surfaces. An approach to the quantification of gradient structures is pointed out. Finally, we treat the difficult case of TEM of thin foils, showing how simple measurements in the projection plane can yield usable estimates of such quantities as the number per unit volume, volume fraction, and the particle density per unit area on vertical or inclined boundaries.

ACKNOWLEDGMENTS

The authors would like to acknowledge the contributions of graduate students E. Y. Chen, E. H. Chia, K. H. Chien, E. J. Coyne, Jr., Fu-Shiong Lin, R. E. Sanders, Jr. and B. Sarkar for supplying the micrographs. Financial support by the U. S. Air Force Office of Scientific Research under Grant No. AFOSR-78-3471 and the Office of Naval Research under Contract N00014-75-C-0349 during the writing of the manuscript is greatly appreciated.

REFERENCES:


1. Underwood, E.E., Quantitative Stereology, Addison-Wesley Publ. Co., Reading, Mass. 1970.

2. Passoja, D.E., and Hill, D.C., Fractography-Microscopic Cracking Processes, ASTM STP 600, American Soc. for Testing Mats., 1976, pp. 30-46.

3. Kocks, U.F., Philosophical Magazine, Vol. 13, 1966, p. 541.

4. Sanders, R. E., Jr. and Starke, E. A. Jr., Materials Science and Engineering, Vol. 28, 1977, pp. 53-68.

5. Sanders, R. E. Jr. and Starke, E. A. Jr., "The Effect of Intermediate Thermo-mechanical Treatments on the Fatigue Properties of a 7050 Al Alloy," Metallurgical Transactions (in press).

6. Fine, M.E., Annual Tech. Report, Relation of Structure of Fatigue Properties in Aluminum-Base Alloys, AF Grant No. AFOSR-76-2892A, 10 Nov. 1977

7. Chien, K. H. and Starke, E. A., Jr., Acta Metallurgica, Vol. 23, 1975, pp. 1173-1184.

8. Underwood, E. E., Journal of Microscopy, Vol. 95, Parts 1 and 3, 1972, p. 25.

9. Uchimoto, T., Sakamoto, A. and Nagata, S., Quantitative Evaluation of Electron-fractography of Fatigue Fracture Surface, Transactions, ISIJ, Vol. 17, No.3, 1977, p.1.

10. Bates, R. C. and Clark, W. G., Jr., Transactions American Society for Metals, Vol. 62, 1969, p. 386.

11. Camard, P., Chermant, J.L., and Coster, M. Morphology of an Imbricate Structure, in Quantitative Analysis of Microstructures in Materials Science, Biology and Medicine, edited by J. L. Chermant, Dr. Riederer-Verlag GmbH, Stuttgart, 1978, p. 126.

12. Bathias, C. and Pelloux, R. M., Metallurgical Transactions, Vol. 4, 1973, p. 1265.

13. Pickens, J.R. and Gurland, J., Metallographic Characterization of Fracture Surface Profiles on Sectioning Planes, Proceedings, Fourth International Congress for Stereology, NBS Spec. Publ. 431, edited by E.E. Underwood, R. deWit, and G.A. Moore, 1976, p. 269.

14. Underwood, E. E. and Coons, W. C., Deformation Twinning, edited by R. E. Reed-Hill, J. P. Hirth, and H. C. Rogers, Gordon and Breach, New York, 1964, p. 405.

15. Flinn, J. E., and Philofsky, E. M., Transactions, American Society for Metals, Vol. 61, 1968, p. 37.

16. Chen, E. Y., and Starke, E. A., Jr., Materials Science and Engineering, Vol. 24, 1976, pp. 209-221.

17. Chia, E. Henry, and Starke, E. A. Jr., Metallurgical Transactions, Vol. 8A, 1977, pp. 825-832.